Research Article | Vol. 62, No. 30 / 20 October 2023 / Applied Optics 7917

applied optics

Verification of different Fizeau fringe analysis algorithms based on airborne wind lidar data in support of ESA's Aeolus mission

BENJAMIN WITSCHAS,[1,*] MICHAEL VAUGHAN,[2] OLIVER LUX,[1] CHRISTIAN LEMMERZ,[1] INES NIKOLAUS,[3] AND OLIVER REITEBUCH[1]

[1]Deutsches Zentrum für Luft- und Raumfahrt e.V. (DLR), Institut für Physik der Atmosphäre, 82234 Oberpfaffenhofen, Germany
[2]Optical & Lidar Associates (OLA), Buckinghamshire, HP14 3PF, UK
[3]University of Applied Sciences Munich, Munich, Germany
*Benjamin.Witschas@dlr.de

Received 9 August 2023; revised 25 September 2023; accepted 25 September 2023; posted 26 September 2023; published 11 October 2023

The Aeolus mission by the European Space Agency was launched in August 2018 and stopped operations in April 2023. Aeolus carried the direct-detection Atmospheric LAser Doppler INstrument (ALADIN). To support the preparation of Aeolus, the ALADIN Airborne Demonstrator (A2D) instrument was developed and applied in several field campaigns. Both ALADIN and A2D consist of so-called Rayleigh and Mie channels used to measure wind from both molecular and particulate backscatter signals. The Mie channel is based on the fringe-imaging technique, which relies on determining the spatial location of a linear interference pattern (fringe) that originated from multiple interference in a Fizeau spectrometer. The accuracy of the retrieved winds is among others depending on the analytic algorithm used for determining the fringe location on the detector. In this paper, the performance of two algorithms using Lorentzian and Voigt fit functions is investigated by applying them to A2D data that were acquired during the AVATAR-I airborne campaign. For performance validation, the data of a highly accurate heterodyne detection wind lidar (2-µm DWL) that was flown in parallel are used as a reference. In addition, a fast and non-fit-based algorithm based on a four-pixel intensity ratio approach (R_4) is developed. It is revealed that the Voigt-fit-based algorithm provides 50% more data points than the Lorentzian-based algorithm while applying a quality control that yields a similar random error of about 1.5 m/s. The R_4 algorithm is shown to deliver a similar accuracy as the Voigt-fit-based algorithms, with the advantage of a one to two orders of magnitude faster computation time. Principally, the R_4 algorithm can be adapted to other spectroscopic applications where sub-pixel knowledge of the location of measured peak profiles is needed.

https://doi.org/10.1364/AO.502955

1. INTRODUCTION

The Aeolus mission by the European Space Agency (ESA) was launched in August 2018 and completed its successful mission time of more than 4.5 years by the end of April 2023, exceeding its planned mission lifetime by 18 months. Finally, Aeolus reentered the Earth's atmosphere on 28 July 2023. The Aeolus satellite carried a single payload: the direct-detection Atmospheric LAser Doppler INstrument (ALADIN), and circled the Earth on a Sun-synchronous orbit at about 320 km altitude, with a repeat cycle of 7 days [1–4]. By exploiting the Doppler shifts that the transmitted ultraviolet laser pulses experienced when they were backscattered from molecules, aerosols, and clouds, Aeolus provided profiles of the wind vector component along the instrument's line-of-sight (LOS) direction from the ground up to about 30 km in the stratosphere [5–7], primarily aiming to improve numerical weather prediction (NWP) [8–13]. In particular, wind profiles acquired over the Southern Hemisphere, the tropics, and the oceans contributed to closing large gaps in the availability of wind data in the global observing system [14].

To support the preparation of Aeolus, the ALADIN Airborne Demonstrator (A2D) instrument with the same measurement principle and similar specifications was developed [15,16] and applied onboard the German Aerospace Center's (Deutsches Zentrum für Luft- und Raumfahrt, DLR) research aircraft Falcon, in several field campaigns before [17–19] and after [20–23] the launch of the satellite. Both ALADIN and A2D consist of so-called Rayleigh and Mie channels used to measure wind from both molecular and particulate backscatter signals. The measurement of Mie-channel winds is based on the fringe-imaging technique [24], which relies on determining the spatial location of a linear interference pattern (fringe) formed by a Fizeau spectrometer. The linear fringe is imaged onto the Mie-channel detector and is afterwards vertically integrated into a 1D profile. The spatial location of the fringe is proportional to the LOS wind speed. The accuracy of these so-called Mie winds, derived from the Doppler shift of the aerosol and cloud backscatter thus depends on several pre- and post-detection factors. These include the optical quality of the Fizeau interferometer, its illumination properties, any spurious background light, the number of detector pixels, as well as the algorithm used for determining the fringe location on the detector. In the Aeolus Level 1B (L1B) [25] and Level 2B (L2B) [26] processor and also for the A2D, the centroid location and the width of the Fizeau fringes are usually analyzed by the so-called Mie-core 2 algorithm, which applies a downhill simplex fit routine of a Lorentzian peak function to the measurement fringe data. Although this algorithm works accurately and reliably, recent investigations based on Aeolus and A2D ground return signals demonstrated that the Mie fringe profile is better described by a Voigt profile. Thus, the application of a Voigt fit should improve the frequency measurement and the accuracy of the retrieved scattering ratio. For this reason, a Voigt fit was implemented in the Aeolus L1B processor in 2022, primarily to improve the quality of the retrieved ratio of the backscatter coefficients of the total backscatter from particles and molecules to the backscatter from molecules (scattering ratio). In the future, it is foreseen to test if this algorithm also improves the quality of the Mie fringe centroid computation.

For the two fit-based approaches, the signal of the entire signal across the 16-pixel wide detector is used. Considering the Fizeau fringe width of about 195 MHz and the spectral width of about 100 MHz for one detector pixel, the majority of the Mie signal is distributed over only a few pixels, whereas the other ones mainly contain noise and solar background signal. For instance, four pixels around the Fizeau fringe center contain about 84% of the overall signal contained in the fringe. With this in mind, an alternative algorithm based on an intensity ratio of four pixels was developed (R_4), which is insensitive to uniform background illumination. Furthermore, the R_4 algorithm reduces the computation time by one to two orders of magnitude. This is especially beneficial for the analysis of large data sets as it has for instance been done by Lux *et al*. [27] to determine the Aeolus laser frequency stability in space based on single laser pulse analysis.

The challenge of estimating the parameters of a peak-shaped function is by no means restricted to wind lidar applications but is prominent for spectroscopic applications in general. For instance, Fizeau-interferometer-based wavemeters [28], used to accurately measure and stabilize the frequency of laser light [29], typically image several fringes onto the detector, enabling the application of fast-Fourier analysis methods or other advanced digital filter techniques [30] to determine the period and phase of the quasi-sinusoidal fringe pattern, and with that, to measure the frequency of light. Another example is astronomy measurements, where accurate information about the peak profile is required to determine the wavelength of the acquired Doppler-broadened emission or absorption lines. To this end, the observational data are usually fitted with specific peak profiles by least square procedures or other optimization techniques [31]. Alternatively, especially when the spectral shape of the actual peak profile is unknown, center-of-gravity or weighted center-of-gravity calculations are used for centroid determination [32]. Also for the accurate analysis of periodograms, for instance, to determine the frequency of tones, peak finding algorithms with a sub-pixel accuracy are required. For this purpose, Jacobsen and Kootsookos [33] introduced a fast algorithm that is based on an intensity ratio calculation by using three pixels. This approach is similar to the one used to derive the R_4 algorithm, but has slightly different properties. Hence, the R_4 algorithm can be considered as a modification of the algorithm introduced by Jacobsen and Kootsookos with particular adaptions to the instrumental layout of Aeolus and the A2D. Still, it is not only of relevance for wind lidar retrievals based on the fringe imaging technique, but can be applied in a much broader context.

In this paper, the usually used Lorentzian-fit-based algorithm, the Voigt-fit-based algorithm, as well as the novel R_4 algorithm are introduced and applied to A2D data that were acquired during the AVATAR-I (Aeolus Validation Through Airborne Lidars in Iceland) campaign conducted over Iceland in 2019 [21,23]. The accuracy and precision of the wind speeds retrieved with the different algorithms are evaluated by comparing to data obtained by a heterodyne detection wind lidar system (2-μm DWL) [34–36], which was operated as a reference system also onboard the DLR Falcon aircraft. In Section 2, both the ALADIN and the A2D instrument are introduced with a focus on the receiver of the system, and in particular on the Mie channel. Furthermore, a short overview of the 2-μm DWL is given. Subsequently, in Section 3, the AVATAR-I campaign and the data sets used in this study are introduced. In Section 4, the different Mie fringe analysis algorithms are described, and the different quality control schemes that are applied to the different algorithms are presented in Section 5. In Section 6, the equations used to quantify the quality of A2D Mie winds by means of a statistical comparison against reference data are introduced. The results obtained from these comparisons are discussed in Section 7. First, it is investigated how the respective algorithms perform when being applied to A2D instrument calibration measurement data (Section 7.A). Afterwards, the quality of the retrieved Mie winds is investigated with A2D data that were acquired during a flight performed on 16 September 2019 (Section 7.B), and with data from all 10 flights performed during the AVATAR-I campaign (Section 7.C). The presented results are of relevance for improving the Aeolus Mie wind data quality for upcoming re-processed data sets.

2. INSTRUMENT DESCRIPTION

A. ALADIN

The Aeolus satellite carries a single payload: the direct-detection wind lidar ALADIN. A sketch of the instrumental setup of ALADIN is given in Fig. 1, where the attention is directed to the receiver of the system, and in particular to the Mie channel. A more detailed description of ALADIN is given in [2,16,37], and the laser transmitters, as well as their frequency stability

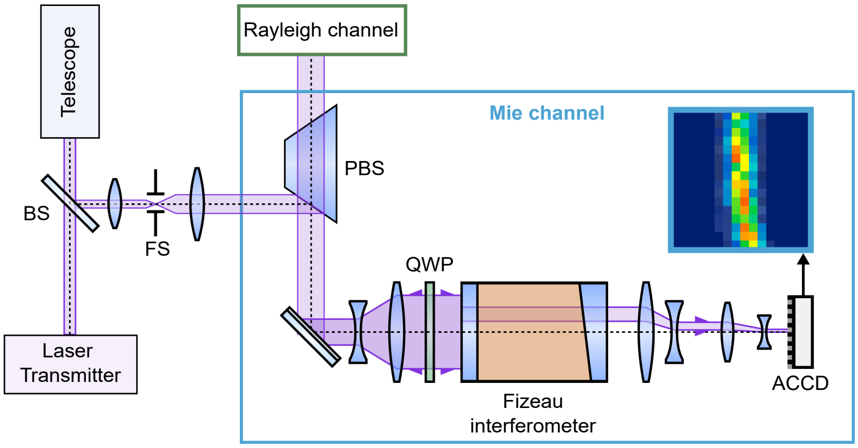

Fig. 1. Simplified sketch of the ALADIN and A2D optical receiver layout reproduced from Lux *et al*. [27]. BS, beam splitter; FS, field stop; PBS, polarizing beam splitter; QWP, quarter-wave plate; ACCD, accumulation charge-coupled device. A 2D image of the Fizeau fringe from the internal reference signal imaged on the 16 × 16 pixel ACCD is indicated.

in space, are discussed by Lux *et al*. [27,38]. A dedicated study about the analysis of the instrument spectral stability of the interferometers in space is reported by Witschas *et al*. [39].

To measure the LOS wind, ultraviolet ($\lambda = 354.8$ nm in vacuum) laser pulses with a pulse energy of 41–101 mJ (depending on the respective laser transmitter and the mission period) are emitted into the atmosphere via a 1.5-m Cassegrain telescope. The laser pulses are generated by means of a diode-pumped, frequency-tripled, and injection-seeded Nd:YAG laser. A small portion of the laser radiation that is leaking through the beam splitter (BS) is used as an internal reference signal (not shown in Fig. 1). This allows the monitoring of the frequency and intensity of the outgoing laser pulses as well as measurements of the frequency-dependent transmission curves of the interferometers. The backscattered radiation from the atmosphere and the ground is collected by the same telescope that is used for emission (mono-static configuration) and directed through a field stop (FS) with a diameter of about 88 µm to set the field of view of the receiver to be only 18 µrad. This is needed to limit the influence of solar background radiation and to account for the angular sensitivity of the spectrometers. Afterwards, the light is reflected on a polarizing beam splitter (PBS) and directed to a beam expander, which increases the beam diameter to 36 mm to reduce its divergence to 555 µrad, before it is sent through the Fizeau interferometer. The Fizeau interferometer acts as a narrow-band filter with an effective full width at half maximum (FWHM) of about 83 fm (195 MHz) and is used to analyze the frequency shift of the narrow-band Mie backscattered light from aerosols and clouds. The Fizeau interferometer spacer is made of Zerodur to benefit from its low thermal expansion coefficient. It is composed of two reflecting plates separated by 68.5 mm, leading to a free spectral range (FSR) of 0.92 fm (2190 MHz) and an effective finesse of about 11.2, where the finesse is defined as the ratio of the FSR and the effective FWHM. The plates are tilted by 4.77 µrad with respect to each other, and the space in between is evacuated. The Fizeau fringes are imaged onto an accumulation charge-coupled device (ACCD) in different pixel columns depending on the laser frequency, as they were formed by constructive interference of the multiple reflected beams at different lateral positions along the tilted plates. The quadratic imaging zone of the ACCD does not image the entire spectral range covered by the Fizeau circular aperture, but only a part of 0.69 fm (1577 MHz), which is called the useful spectral range. This so-called fringe imaging technique using a Fizeau interferometer [24] was specially developed for ALADIN [1]. The light reflected from the Fizeau interferometer is directed towards the Rayleigh channel to analyze the frequency shift of the broad-band molecular scattered light by means of the so-called double-edge technique [40,41]. Both the Rayleigh and Mie channels sample the backscatter signal time-resolved to 24 bins with a vertical resolution between 0.25 and 2.0 km. The horizontal resolution of the wind observations is about 90 km for the Rayleigh channel and down to 10 km for the Mie channel with overall sub-sample information on a 3-km scale.

B. ALADIN Airborne Demonstrator

The A2D has a very similar architecture to ALADIN (Fig. 1), and thus represents an ideal test-bed for ALADIN performance investigations. The laser pulses produced by the A2D laser transmitter have an energy of about 60 mJ, a duration of about 20 ns (FWHM), and a 50-Hz repetition rate. In contrast to ALADIN, which incorporates a 1.5-m-diameter telescope and operates at an off-nadir pointing angle of 35°, the A2D employs a 0.2-m telescope, which is oriented at an off-nadir angle of 20°. Furthermore, the A2D is based on a bi-static design, meaning that the laser pulses are emitted via a piezo-electrically controlled mirror that is attached to the frame of a Cassegrain-type telescope. The rest of the A2D receiver chain is identical to the one of ALADIN, except for particular front optics that take care of the different operating altitude ranges for both instruments. Although the detection scheme for the A2D is similar to the one of ALADIN, the horizontal resolution of the wind data is higher, namely, about 3.6 km for both channels, due to the lower ground speed of the aircraft (≈ 200 m/s) compared to Aeolus (≈ 7200 m/s). A detailed description of the A2D can be found in [16,18].

C. 2-μm Doppler Wind Lidar

For the validation of the accuracy and precision of A2D winds, the 2-μm DWL is operated as a reference instrument in parallel. It has been deployed by DLR since 1999 and has been applied in several field campaigns to measure the horizontal wind speeds over the Atlantic Ocean as input data for numerical weather prediction assimilation experiments [34,42], and also to characterize the optical properties of aerosols [43]. For the last 5 years, the major task of the 2-μm DWL was the validation of Aeolus [20–23]. Additionally, the system was used to study the occurrence and spectral characteristics of orographically induced gravity waves [35,36,44,45].

The 2-μm DWL is based on a Tm:LuAG laser, producing laser pulses with a wavelength of 2022.54 nm (vacuum), 1–2-mJ energy, a width of about 400 ns (FWHM), and a repetition rate of 500 Hz. Together with a diameter of about 10 cm of the transmitted laser beam, the system provides eye-safe operation. Furthermore, the system is equipped with a double-wedge scanner unit, enabling it to measure not only the LOS wind speed but the entire wind vector while applying the velocity-azimuth display scan technique [46]. Contrary to ALADIN and A2D, the 2-μm DWL is based on a heterodyne detection measurement principle, meaning that the signal backscattered from the atmosphere is mixed with a local oscillator laser source that is also used as a seed laser. The Doppler frequency shift between the outgoing laser pulse and the backscattered light results in a beat signal that is proportional to the LOS wind speed. As this principle relies on a narrow bandwidth, it only works for light scattered on particles. However, due to the very high sensitivity, large data coverage is usually reached in atmospheric conditions that are considered cloud- and aerosol-free by the Rayleigh channel of ALADIN and A2D. The vertical resolution of 2-μm DWL data is ≈ 100 m, restricted by the laser pulse length. The horizontal resolution of wind vector measurements is ≈ 8.4 km considering the time for one scan of 42 s and the usual aircraft ground speed of 200 m/s. More information about the 2-μm DWL instrumental setup and processing schemes is provided in Witschas *et al*. [35,36]. An in-depth overview of the principle of heterodyne-detection wind lidars is given in [47].

3. AVATAR-I CAMPAIGN

As one out of four airborne Aeolus calibration and validation campaigns [20–22,48], the AVATAR-I campaign was performed from 9 September until 1 October 2019 in Keflavik, Iceland [36,48]. During AVATAR-I, DLR operated the Falcon aircraft equipped with both the A2D and the 2-μm DWL. While the 2-μm DWL data were mainly used to validate the quality of the Aeolus L2B wind product [21], A2D data were used to optimize the Aeolus wind retrieval and calibration procedures [48]. A total of 10 Aeolus underflights were performed, covering about 8000 km of the Aeolus measurement track. Furthermore, two particular A2D calibration flights were conducted as discussed in Section 7.A. An overview of all flight tracks is given in Fig. 2. Additional information about the overall duration of the respective flights, the start and stop times, and the corresponding geolocations of the Aeolus underflight can be found in Table 2 in [21].

4. FIZEAU FRINGE ANALYSIS ALGORITHMS

A. Fit-Based Algorithms

Considering the small wedge angle of 4.77 μrad, and the relatively low effective finesse of about 11.2, the transmission function of the ALADIN and A2D Fizeau interferometers is not remarkably affected by asymmetry effects and can be described

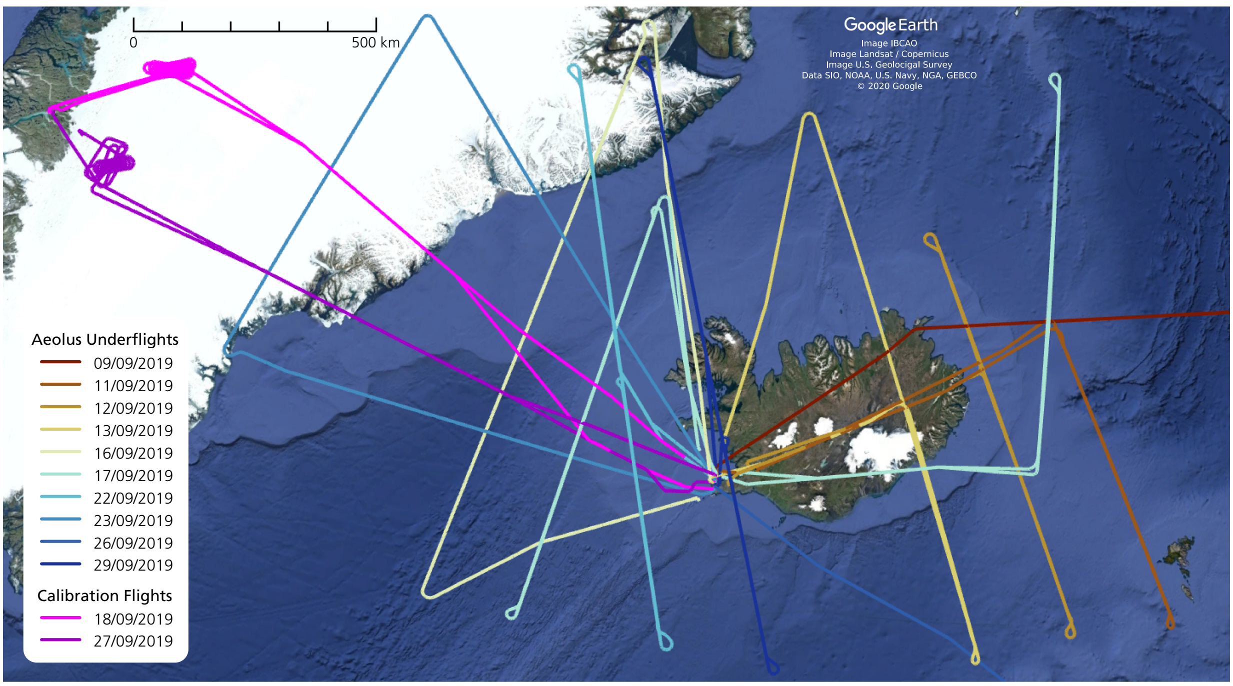

Fig. 2. Flight tracks of the Falcon aircraft during the AVATAR-I campaign in September 2019. Each color represents a single flight. Purple and magenta lines indicate the tracks of particular A2D calibration flights with circles above Greenland.

by a Lorentzian peak function according to [49–51]

$$\mathcal{L}(x) = I_{\mathcal{L}} \cdot \frac{\Gamma_{\mathcal{L}}^2}{4(x-x_0)^2 + \Gamma_{\mathcal{L}}^2}, \tag{1}$$

where $I_{\mathcal{L}}$ is the peak height, $\Gamma_{\mathcal{L}}$ is the FWHM of the Lorentzian peak profile, and x_0 is the center position. In the Aeolus processor, Eq. (1) is used in a downhill simplex fitting algorithm to determine the Fizeau fringe position and width [15,17,25] to finally derive the Doppler shift of the narrow-band backscattered light and hence, the LOS wind speed.

However, after a more careful analysis of the measured A2D and ALADIN fringes, it turned out that the fringe profile is better described by a Voigt function that is represented as the convolution of a Lorentzian $\mathcal{L}$ and a Gaussian $\mathcal{G}$ peak profile according to [52]

$$\mathcal{V}(x) = I_{\mathcal{V}} \left({\mathcal{G}_{\mathcal{V}}}^{\mathrm{N}} * {\mathcal{L}_{\mathcal{V}}}^{\mathrm{N}} \right)(x), \tag{2}$$

where * denotes the convolution, $I_{\mathcal{V}}$ is the area below the peak, and ${\mathcal{L}_{\mathcal{V}}}^{\mathrm{N}}(x)$ and ${\mathcal{G}_{\mathcal{V}}}^{\mathrm{N}}(x)$ are normalized to unit area according to

$${\mathcal{L}_{\mathcal{V}}}^{\mathrm{N}}(x) = \frac{2}{\pi} \cdot \frac{\Gamma_{\mathcal{L}}}{4(x-x_0)^2 + \Gamma_{\mathcal{L}}^2} \tag{3}$$

and

$${\mathcal{G}_{\mathcal{V}}}^{\mathrm{N}}(x) = \frac{\sqrt{4\ln 2}}{\sqrt{\pi}\Gamma_{\mathcal{G}}} \exp\left(-\frac{4\ln 2}{\Gamma_{\mathcal{G}}^2}(x-x_0)^2 \right), \tag{4}$$

with $\Gamma_{\mathcal{L}}$ and $\Gamma_{\mathcal{G}}$ being the FWHM of the Lorentzian and the Gaussian peak profile, respectively. Hence, a second effect with a Gaussian spectral distribution causes deviation from the ideal Lorentzian peak profile. Sophisticated wave optic analysis simulations [53] have revealed that an off-axis illumination of the Fizeau interferometer of ≈ 100 µrad with a divergent laser beam (≈ 500 µrad) can explain the observed Voigt shape of the A2D and Aeolus Mie fringes (not shown).

As the convolution given by Eq. (2) has no analytical solution, the pseudo-Voigt approximation is used instead as a linear combination of the Lorentzian $\mathcal{L}^{\mathrm{N}}(x)$ and Gaussian $\mathcal{G}^{\mathrm{N}}(x)$ peak functions according to

$$\mathcal{V}(x) = I_{\mathcal{V}} \left(\eta \mathcal{G}^{\mathrm{N}}(x) + (1-\eta)\mathcal{L}^{\mathrm{N}}(x) \right), \tag{5}$$

where η is a weighting parameter that can vary between zero and one, and the Lorentzian and a Gaussian peak profile do now have a similar FWHM $\Gamma_{\mathcal{V}}$, which is also the FWHM of the pseudo-Voigt profile. Consequently, they are written as

$$\mathcal{L}^{\mathrm{N}}(x) = \frac{2}{\pi} \cdot \frac{\Gamma_{\mathcal{V}}}{4(x-x_0)^2 + \Gamma_{\mathcal{V}}^2} \tag{6}$$

and

$$\mathcal{G}^{\mathrm{N}}(x) = \frac{\sqrt{4\ln 2}}{\sqrt{\pi}\Gamma_{\mathcal{V}}} \exp\left(-\frac{4\ln 2}{\Gamma_{\mathcal{V}}^2}(x-x_0)^2 \right). \tag{7}$$

The normalized peak functions ($\mathcal{G}^{\mathrm{N}}(x)$ and $\mathcal{L}^{\mathrm{N}}(x)$) share two parameters, namely, the peak center position x_0, and the FWHM of the peak $\Gamma_{\mathcal{V}}$. To reduce computation time and to improve the fit convergence, η and $\Gamma_{\mathcal{V}}$ are considered to

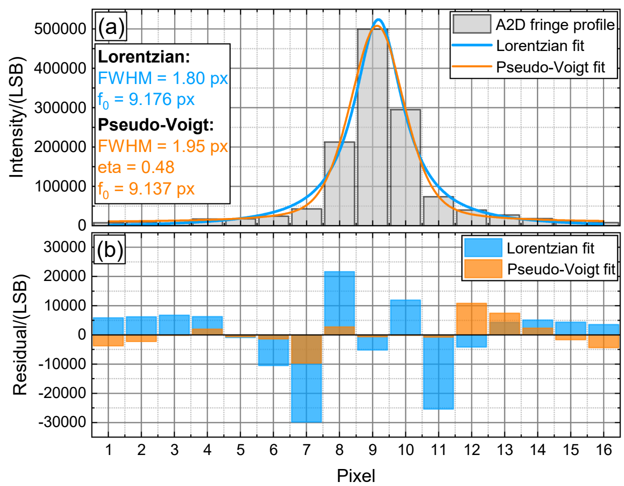

Fig. 3. (a) A2D Mie fringe profile (gray bars) obtained from ground return signals acquired during an airborne calibration measurement performed on 18 September 2019 (see Section 7.A). Best fits of the Lorentzian function according to Eq. (1), and the pseudo-Voigt fit function according to Eq. (5) are indicated by the blue and orange lines, respectively. (b) Corresponding residuals between measurement data, and best fits.

be constant. In particular, fringe profiles from A2D ground returns were analyzed and resulted in values of $\eta = 0.48$ and $\Gamma_{\mathcal{V}} = 1.95$ px. The remaining fit parameters that are optimized in a non-linear Levenberg–Marquardt algorithm are thus x_0 and $I_{\mathcal{V}}$.

In Fig. 3(a), the A2D fringe profile obtained from ground returns acquired during a calibration measurement (see also Section 7.A) is shown by the gray bars. The blue line indicates the best fit of the Lorentzian [Eq. (1)], and the orange line represents the best fit of the pseudo-Voigt function [Eq. (5)], with all parameters free for the fit optimization. The retrieved fit parameters are shown by the inset. In Fig. 3(b), the corresponding residuals are shown.

It is obvious that the accordance of the pseudo-Voigt fit with a sum of least square differences of $3.3 \cdot 10^8$ LSB is noticeably better than for the Lorentzian fit with a sum of least square differences of $2.8 \cdot 10^9$ LSB. The wings of the fringe profile (i.e., around pixels 6–7.5 and 10.5–12) are especially overestimated by the Lorentzian fit, whereas they are adequately represented by the pseudo-Voigt fit. The determined FWHMs are 1.80 px for the Lorentzian and 1.95 px for the pseudo-Voigt fit and hence, differ by about 8.3%. The corresponding center positions are determined to be 9.176 px and 9.137 px, respectively, where the difference of 0.039 px corresponds to a considerable difference in the determined LOS wind speed of about 0.7 m/s. Thus, the ground signal analysis indicates that the pseudo-Voigt function describes the actual Fizeau fringe profile with higher accuracy compared to the Lorentzian and hence, may also lead to a more accurate wind retrieval. This hypothesis is proven by means of A2D data analysis as discussed in Section 7.

It is worth mentioning that for the analyses discussed here, the intensity measured within each pixel is treated as an infinitesimal data point and not as a width integral. As revealed by Hagen *et al.* [54] based on the analysis of a Gaussian peak profile with a maximum likelihood approach, this approximation can induce biases in the retrieved peak amplitude and peak width in case the intensity is not varying linearly along the detector pixel. However, they also demonstrate that the determined center position is not affected and remains unbiased. It is further mentioned that in the case of using a spectral pixel width that is approximately as large as the width of the detected peak profile (as is the case for ALADIN and A2D), the originating bias of the determined amplitude and width is small, and has less impact on the uncertainty than a potential discrepancy between the used model function (e.g., pseudo-Voigt function) and the real spectral peak shape. As it can be assumed that these results also hold for Lorentzian and pseudo-Voigt peak profiles, it is concluded that the actual pixel width does not have to be considered for this study.

B. Novel R_4 Algorithm

For the two fit-based approaches, the signal of all 16 pixels is typically used. Considering the Fizeau fringe width of about 195 MHz, the main signal is distributed over only a few pixels, whereas the other ones mainly contain noise and a non-perfectly corrected background signal originating from solar radiation as well as from the broadband Rayleigh backscatter signal. For instance, four pixels around the Fizeau fringe center contain about 84% of the overall signal. With this in mind, it was investigated if the determination of the Fizeau fringe position can be improved by exploiting the information of the four pixels with the highest intensity only. Such an algorithm is also supposed to be less sensitive to the accurate knowledge of the actual fringe profile, which is difficult to measure from space due to the variable Rayleigh signal contribution in the ground signal and the uncertainty that is induced by the correction of the illumination function. In addition, as the Fizeau fringe profile can be assumed to be stable over time, a non-fit-based algorithm reduces the computation time significantly.

Considering that, a novel algorithm based on an intensity ratio approach was developed. In particular, a response function R_4 that describes the fringe position between two adjacent pixels is calculated according to

$$R_4 = \frac{(I_{p_1} + I_{p_2}) - (I_{p_3} + I_{p_4})}{(I_{p_2} + I_{p_3}) - (I_{p_1} + I_{p_4})}, \tag{8}$$

where I_{p_x} is the signal intensity measured at the pixel p_x, and x represents the respective pixel number of the ACCD detector. The lower index of the two neighboring pixels with the highest intensity is defined to be p_2. Thus, $R_4 = 1$ in case the fringe is centered at p_2, $R_4 = 0$ in case the fringe is in between p_2 and p_3, and $R_4 = -1$ in case the fringe is centered at p_3. The fringe positions of these three edge cases are sketched in Fig. 4.

To verify the performance of the R_4 algorithm and to investigate its sensitivity to the accurate knowledge of the actual fringe profile, simulations with different Fizeau fringe shapes were performed. In particular, a Lorentzian profile according to Eq. (3) with $\Gamma_{\mathcal{L}} = 150$ MHz, and four Voigt profiles according to Eq. (2) with on overall FWHM of 150 MHz, 165 MHz, 185 MHz, and 200 MHz are used as they are depicted in Fig. 5(a). For a better visualization of the differences between the simulated fringes, they are also plotted with a logarithmic y-axis [Fig. 5(b)]. The actual ratio of the FWHM of the Lorentzian ($\Gamma_{\mathcal{L}}$) and the Gaussian ($\Gamma_{\mathcal{G}}$) contribution to the respective Voigt profile is summarized in Table 1.

The fringe profiles are simulated with a spectral resolution of 1 MHz (lines), normalized to unit area, and afterwards binned to a spectral resolution of 100 MHz (bars), which corresponds to the spectral pixel width of the ACCD.

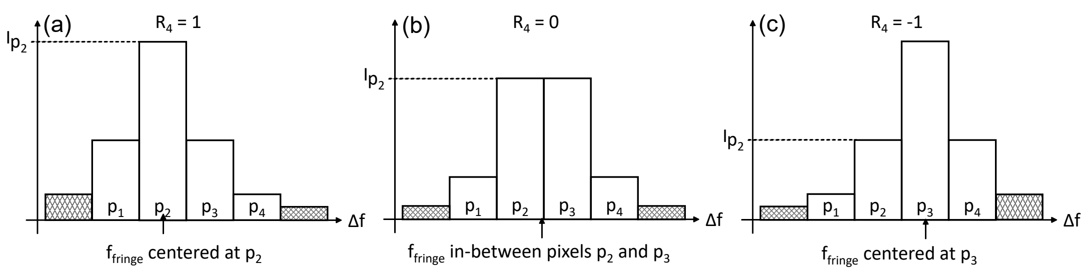

Fig. 4. Fizeau fringe intensity distribution for three edge cases having the fringe centered (a) at pixel 2, (b) in between pixel 2 and pixel 3, and (c) at pixel 3, leading to R_4 values of one, zero, and −1, respectively.

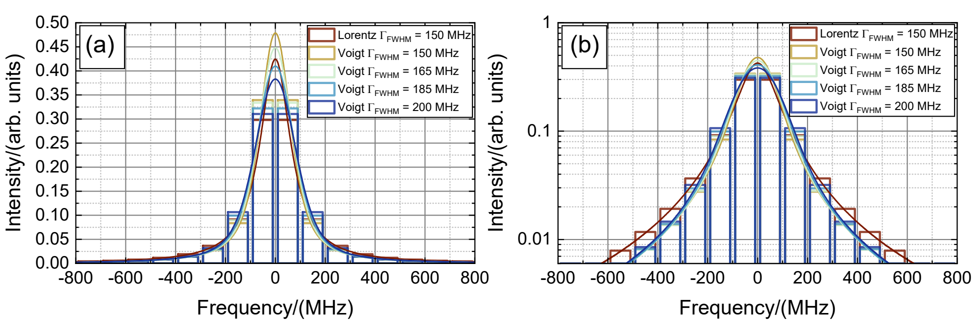

Fig. 5. (a) Five different Fizeau fringe profiles with 1-MHz spectral resolution (lines) and 100-MHz (bars) as used for simulations. Details of the respective fringe profile functions are given in Table 1. Each fringe profile is normalized to unit area. (b) Same data as in the left panel, but with a logarithmic y-axis.

Table 1. Overview of Fizeau Fringe Profiles Used for R_4 Simulations

Fringe Profile	$\Gamma_{\mathcal{L}}$/(MHz)	$\Gamma_{\mathcal{G}}$/(MHz)	$\Gamma_{\mathcal{V}}$/(MHz)
Lorentz	150	–	150
Voigt I	100.8	83.9	150
Voigt II	98.5	102.6	165
Voigt III	98.5	124.2	185
Voigt IV	101.5	137.9	200

Based on these idealized fringe profiles, the R_4 values originating for a fringe location varying between two pixels are simulated. To this end, the binned fringe profiles (Fig. 5, colored bars) are then frequency-shifted in 1-MHz steps over a frequency range of 100 MHz, which corresponds to a fringe movement of one pixel, and finally, the R_4 value is calculated at each frequency step as it is shown in Fig. 6(a). In Figs. 6(b) and 6(c), the residuals to a line fit and to a fifth-order polynomial fit that only considers odd terms are depicted, respectively.

Analyzing the residual to the line fit [Fig. 6(b)], it can be seen that R_4 varies almost linearly between two pixels. The peak-to-peak variation is about ± 4 MHz (± 0.04 pixels) for all fringe profiles. It is also interesting to note that the difference between the different Voigt profiles is only ± 0.7 MHz (± 0.007 pixels), demonstrating the insensitivity of the R_4 algorithm to the accurate knowledge of the actual fringe profile. The residual to a fifth-order polynomial fit that only considers odd terms varies by less than ± 0.05 MHz for all fringe profiles. Thus, a fifth-order polynomial fit is suitable to be used to describe the relationship between the calculated R_4 value and the actual fringe position between two pixels. In particular, the fringe position (in pixels) $\mathcal{F}_{\text{center}}$ is calculated according to

$$\mathcal{F}_{\text{center}} = 0.5 + p_2 + \left(A1 \cdot R_4 + A2 \cdot R_4{}^3 + A3 \cdot R_4{}^5\right), \quad \text{(9)}$$

where p_2 is the pixel index, and $A1$, $A2$, and $A3$ are constants determined by simulations. This is also the point where assumptions about the fringe profile must be made. However, as mentioned before, the R_4 algorithm is only marginally dependent on the actual shape of the fringe profile. For the A2D analysis, as discussed in Section 7, a pseudo-Voigt profile with an FWHM of 185 MHz is considered, leading to $A1 = -0.6068$, $A2 = 0.1402$, and $A3 = -0.03373$.

It is worth mentioning that the performances of other algorithms based on intensity ratios defined as $R_3 = (I_{p_1} - I_{p_3})/(2 \cdot I_{p_2} - (I_{p_1} + I_{p_3})$ and $R_6 = [(I_{p_5} + I_{p_6}) - (I_{p_2} + I_{p_3})]/(I_{p_1} - I_{p_4})$ were investigated by means of simulations. R_3 and R_6 also range between -1 and 1 throughout one pixel and share the property of being insensitive to a uniformly distributed background signal. However, in contrast to R_4, they are less linear and more dependent on the accurate knowledge of the underlying fringe profile. Hence, for the underlying problem, the R_4 algorithm is considered the best option, but other intensity ratios can be principally defined if required.

5. DATA QUALITY CONTROL

The Mie fringe analysis algorithms introduced in Section 4 are usually applied to every observation (signal average over 14 s) and range gate available for A2D data. Hence, a quality control (QC) scheme is additionally needed to exclude invalid data points with an insufficient signal-to-noise ratio (SNR). Due to the different nature of the respective algorithms, different QC options with different thresholds have to be applied. For a meaningful comparison of the actual performance of the algorithms, the QC thresholds are chosen such that the comparison of A2D against reference data yields a similar random error. The number of retrieved valid data points is then considered as a measure of the quality of each algorithm.

For the Lorentzian-based fit algorithm, a contrast ratio of the data is used as the QC parameter. It is defined as the ratio of the intensity of the most powerful pixel divided by the sum of the intensities contained in the six outer pixels on each side {see also Eq. (3.29) in Ref. [55]}. In this study, a threshold for the contrast ratio of 3.0 is used. Afterwards, a median filter with a window size of five and a threshold of 8 m/s is applied for final gross outlier removal. The median wind speed within a 5×5 window (observation versus range gate) is calculated, and all data points with a deviation of larger than 8 m/s are excluded. If more than 35% of the data points are valid, the center data point is considered as a valid wind speed. Otherwise, it is deleted.

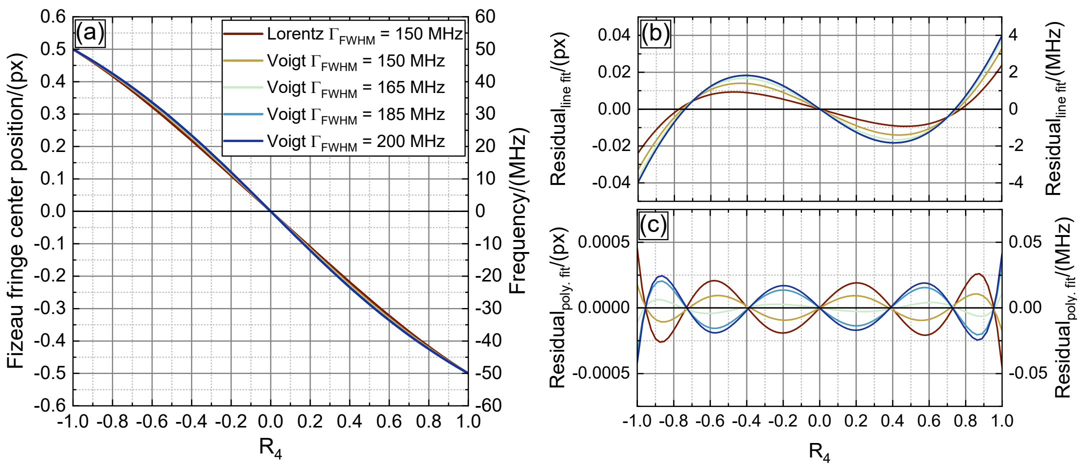

Fig. 6. (a) Fizeau fringe center position varying between ± 50 MHz (± 0.5 pixels), depending on R_4 [Eq. (8)] calculated for the simulated fringe profiles with different FWHM as shown in Fig. 5. (b) Mie fringe center position residual with respect to a linear fit. (c) Mie fringe center position residual with respect to a fifth-order polynomial fit. For the simulation, a pixel width of 100 MHz was used.

Usually, the QC parameters are chosen such that the median filter excludes less than 10% of the data points.

For the pseudo-Voigt fit, the integrated peak intensity I_V obtained from the fit according to Eq. (5) is used as a QC parameter. All observations with I_V smaller than 1000 LSB (least significant bits) are considered to be invalid. Afterwards, a median filter similar to the one used for the Lorentzian fit is applied.

For the R_4 algorithm, all observations that yield an R_4 value smaller than -1 or larger than 1 are defined as invalid. In addition, an intensity threshold is applied. All observations where the sum of the intensities measured on the two pixels p_2 and p_3 is smaller than 600 LSB are excluded. Alternatively, $w_4 = (I_{p_2} + I_{p_3})/(I_{p_1} + I_{p_4})$ as a parameter that is proportional to the fringe width can be derived and used for QC, which is not done in this study. The last step applies a median filter similar to the one used with the other two algorithms.

6. STATISTICAL COMPARISON OF A2D AND 2-μm DWL DATA

The accuracy and precision of the A2D Mie wind results are evaluated by comparing them to the wind data obtained from the 2-μm DWL reference instrument. Due to the different horizontal and vertical resolutions of both data sets, averaging procedures are needed. For this purpose, the 3D wind vectors measured with the 2-μm DWL were projected onto the A2D LOS axis. Moreover, the 2-μm DWL measurement grid was adapted to that of the A2D by means of a weighted aerial interpolation algorithm, as introduced in [56].

To validate the quality of A2D Mie LOS winds ($\mathcal{O}_{\mathrm{LOS}}$) depending on the respective Mie fringe analysis algorithm, the wind velocity difference v_{diff} with respect to the 2-μm DWL reference data projected onto the A2D viewing direction ($\mathcal{R}_{\mathrm{LOS}}$) is calculated according to

$$v_{\mathrm{diff}} = \mathcal{O}_{\mathrm{LOS}} - \mathcal{R}_{\mathrm{LOS}}. \tag{10}$$

The bias μ and standard deviation (STD) σ of v_{diff} are calculated by use of

$$\mu = \frac{1}{n}\sum_{i=1}^{n} v_{\mathrm{diff}} \tag{11}$$

and

$$\sigma = \sqrt{\frac{1}{n-1}\sum_{i=1}^{n} (v_{\mathrm{diff}} - \mu)^2}, \tag{12}$$

where n is the number of available data points. In addition to the STD, the scaled median absolute deviation (scaled MAD) k is calculated according to

$$k = 1.4826 \times \mathrm{median}(|v_{\mathrm{diff}} - \mathrm{median}(v_{\mathrm{diff}})|). \tag{13}$$

The scaled MAD has the advantage that it is less sensitive to single outliers that may result in larger STD values. It is thus used as a measure of the random error of A2D LOS winds. The scalar of 1.4826 is chosen such that k is identical to the standard deviation according to Eq. (12), when the data set is normally distributed. Furthermore, the uncertainty of the bias k_μ is calculated according to

$$k_\mu = \frac{k}{\sqrt{n}}. \tag{14}$$

For the statistical comparison of the two data sets, outliers originating either from the A2D or the 2-μm DWL are defined by means of the modified Z-score

$$\mathrm{Z_{m,i}} = \frac{v_{\mathrm{diff}_i} - \mathrm{median}(v_{\mathrm{diff}})}{k}. \tag{15}$$

In this study, a modified Z-score threshold of 3.5 is used to define outliers, which are not considered for the statistical comparison by means of Eqs. (11)–(14). It is the Z-score threshold value suggested by Iglewicz and Hoaglin [57], which was derived from a simulation study performed with random normal observations and led to an outlier portion of less than 10%.

7. RESULTS

In the following, the performance of the respective fringe analysis algorithms is investigated based on the A2D data acquired during the AVATAR-I campaign. In Section 7.A, data from the calibration flight performed on 18 September 2019 are analyzed and discussed. In Section 7.B, the differences between the fringe analysis algorithms are investigated based on the flight performed on 16 September 2019 as a case study. In Section 7.C, the entire AVATAR-I campaign data set is analyzed.

A. Mie Response Calibration

To relate the actual Mie fringe position on the ACCD detector to the frequency of the backscattered light, the Fizeau interferometer response function has to be measured. For this purpose, a particular calibration measurement—a so-called instrument response calibration (IRC)—is performed [17,55]. During an IRC, the laser frequency is scanned in 25-MHz steps over a frequency range of 1.8 GHz, thus simulating well-defined Doppler shifts of the radiation backscattered from the atmosphere. The contribution of the actual atmospheric wind along the LOS of the instrument is eliminated by pointing the laser to nadir direction and measuring in areas with negligible vertical wind speeds. As the A2D is not equipped with a scanning device, this is accomplished by flying circles at a roll angle of 20°, hence compensating for the fixed off-nadir angle of the A2D. The calibration procedure takes about 24 min in total. In the framework of the AVATAR-I campaign, two research flights were dedicated to IRC measurements (18 September 2019 and 27 September 2019), both flown above the west coast of Greenland, which was covered with ice and hence, provided strong ground return signals due to the high surface albedo of ice in the UV spectral region (see also Fig. 2, magenta and violet lines). An extract of the data from one IRC measurement from the 18 September flight for a frequency range of -500 to 538 MHz is shown in Fig. 7.

Although the Mie responses retrieved by the different algorithms agree well [Figs. 7(a) and 7(b)], distinct differences can be observed from the residual plots [Figs. 7(c) and 7(d)].

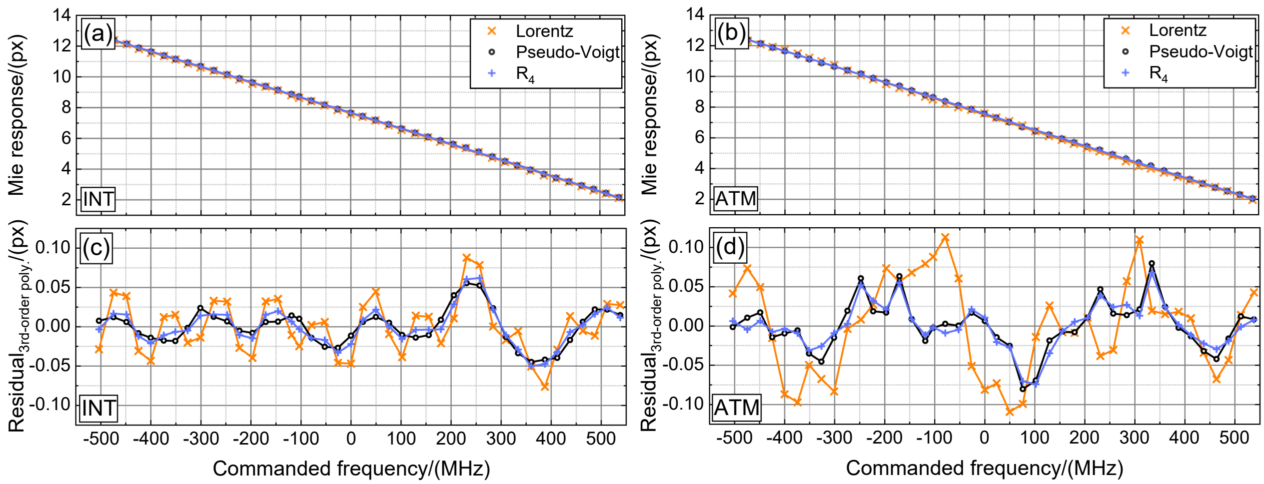

Fig. 7. Mie response of the (a) internal reference signal and (b) ground return signal retrieved by the Lorentzian fit (orange), the pseudo-Voigt fit (black), and the R_4 algorithm (blue), from the calibration data acquired during the flight on 18 September 2019. The corresponding residuals to a third-order polynomial fit are shown in (c) and (d).

The residual is largest for the Lorentzian-fit-based algorithm (orange), reaching peat-to-peak values of about 0.075 px. Considering a sensitivity of 100 MHz/px, this corresponds to ±7.5 MHz or ±1.3 m/s in LOS direction. Furthermore, it can be seen that a pronounced modulation occurs with a frequency of about 100 MHz, which is the spectral distance of the detector pixels (pixelation effect). The residuals of the pseudo-Voigt-fit-based algorithm (black) and the R_4 algorithm (blue) are comparable, reaching peak-to-peak values of about 0.05 px, and are thus, 33% smaller than the Lorentzian one. Furthermore, the imprint of the pixelation effect is less pronounced, indicating that both the pseudo-Voigt algorithm, as well as the R_4 algorithm, determine the actual position of the fringe profiles with better accuracy than the Lorentzian one. For the ground return signals [Figs. 7(b) and 7(d)], the results are generally noisier but reproduce the findings as obtained for the internal reference signal analysis. The Lorentzian-fit-based algorithm (orange) performs worse with peak-to-peak variations of about ±0.1 px, whereas the pseudo-Voigt-fit-based algorithm (black) and the R_4 algorithm (blue) show peak-to-peak variations of less than ±0.075 px and thus, 25% less than for the Lorentzian fit. It is worth mentioning that the variations shown here have been used to adjust the A2D wind retrievals [17]. For ALADIN, NWP model data provide the basis for deviations to a third-order polynomial fit, like those shown in Figs. 7(c) and 7(d) [58].

These results show that both the pseudo-Voigt-based algorithm and also the novel R_4 algorithm increase the accuracy of the Fizeau fringe position determination. Hence, it is also likely that this holds for the retrieved wind speeds as will be discussed in Sections 7.B and 7.C.

B. Wind Measurements on 16 September 2019

To validate the performance of the different fringe analysis algorithms, A2D data from the research flight performed on 16 September 2019 are analyzed (see also Fig. 2). During that flight, the Falcon aircraft took off from Keflavik airport at around 6:45 UTC and headed north-east to about 71°N/26°W, where it entered the Aeolus track. From here, the Falcon flew along the satellite track for about 1000 km, and then headed back to Keflavik airport. The flight was dominated by cloud-free conditions and hence, gives the possibility to investigate the Mie fringe analysis algorithms for moderate SNR conditions. Furthermore, the North Atlantic jet stream, sampled in the southern part of the flight leg between Greenland and Iceland, provided large wind speed gradients for sampling and for comparing the accuracy of the different algorithms across a large portion of the Fizeau useful spectral range. In Fig. 8, the 2-μm DWL 3D wind data projected onto the A2D LOS direction 8(a), together with the A2D Mie winds retrieved by the Lorentzian-based fit algorithm 8(b), the pseudo-Voigt-based fit algorithm 8(c), and the R_4-based algorithm 8(d) are shown. Figs. 8(e)–(g) indicate the differences between the 2-μm DWL data and the respective A2D Mie winds.

It can be seen that the 2-μm DWL provides almost full data coverage during this flight, which is due to the very high sensitivity of the heterodyne detection principle used in the 2-μm DWL. Consequently, the system can measure the wind speed reliably even in regions with low aerosol load. It can also be recognized that the LOS wind speeds extend from about −5 m/s to about 15 m/s. The jet-stream region with LOS wind speeds up to 15 m/s is clearly obvious between 62°N and 66°N in altitudes from about 4 to 8 km. The corresponding A2D Mie winds retrieved with the different algorithms [Figs. 8(b)–8(d)] are in reasonable accordance with the 2-μm DWL data and describe the observed wind pattern reasonably well. However, from the difference plots shown in Figs. 8(e)–8(g), distinct deviations can be observed. For the Lorentzian-based algorithm [Fig. 8(e)], larger positive LOS wind speed differences of up to 5 m/s are present in the jet-stream region. On the other hand, negative deviations of up to −5 m/s are prominent in the northern part of the flight leg. Compared to that, the difference plot of the pseudo-Voigt data [Fig. 8(f)] looks much smoother. Furthermore, it can be seen that valid data points are available in the boundary layer region in the southern part of the flight leg

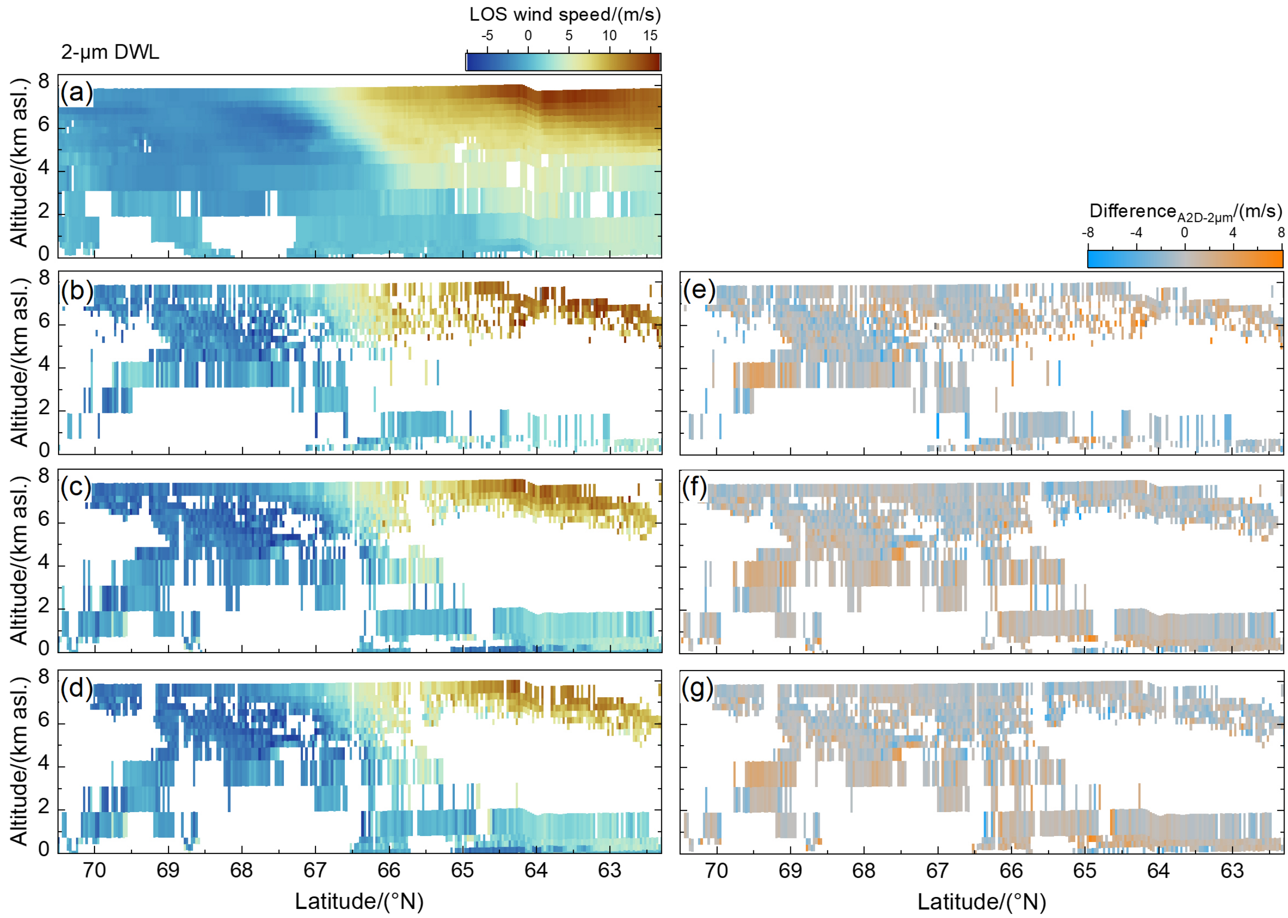

Fig. 8. (a) 2-µm DWL data projected onto the A2D LOS direction, and A2D Mie winds retrieved by the (b) Lorentzian-based fit algorithm, (c) pseudo-Voigt-based fit algorithm, and (d) R_4 algorithm, for the research flight performed on 16 September 2019 during the AVATAR-I campaign. The corresponding differences of the respective A2D Mie winds to the 2-µm DWL data are shown in (e)–(g).

(e.g., 63°N to 65°N), which suggests a higher sensitivity of the pseudo-Voigt algorithm compared to the Lorentzian one. The difference plot for the R_4 data [Fig. 8(g)] looks very similar to the one provided by the pseudo-Voigt fit. Additionally, it can be realized that the overall data coverage is lower compared to the one of the 2-µm DWL, which is due to the different detection principles of both instruments. Because of its high sensitivity, the 2-µm DWL also measures winds in regions with very low aerosol loads that are classified as Rayleigh winds by the A2D (not shown).

For further quantitative verification of the respective Mie-fringe analysis algorithms, a statistical comparison of A2D and 2-µm DWL data is performed as shown in Fig. 9.

For all three algorithms, a reasonable linear relationship with respect to the 2-µm DWL data is evident, although several subtle differences can be observed. The Lorentzian-based algorithm provides 1672 valid wind measurements and 32 outliers (1.9%). The determined bias is (0.71 ± 0.04) m/s and the corresponding random error according to the scaled MAD is 1.52 m/s. Compared to that, the pseudo-Voigt-based algorithm provides 1912 valid wind measurements and hence, an increase of 14%, and 32 outliers (1.7%). The bias is determined to be (-0.91 ± 0.03) m/s and thus, in the same order but with different sign. The random error is 1.27 m/s, and with that, 30% smaller compared to the Lorentzian-based analysis, although the number of valid data points is increased by 14%. This clearly points to a better performance of the pseudo-Voigt-based algorithm. For the R_4-based analysis, 1846 valid wind measurements are retrieved with 29 outliers (1.6%), similar to what was observed by the pseudo-Voigt-based algorithm. This is also true for the retrieved bias and random error, which are (-0.79 ± 0.03) m/s and 1.19 m/s, respectively. Thus, from this analysis, it can be concluded that the pseudo-Voigt-based retrieval performs better than the Lorentzian-based algorithm. The R_4 algorithm performs as well as the pseudo-Voigt-based algorithm and thus, provides a good and especially fast alternative. A summary of the performance of the different Mie fringe analysis algorithms for the flight on 16 September 2019 is given in Table 2.

C. Wind Measurements from the Entire AVATAR-I Campaign Data Set

During AVATAR-I, a total of 10 Aeolus underflights were performed. The corresponding statistical comparison of 2-µm DWL data and A2D data is shown in Fig. 10, where the figure is similarly arranged as Fig. 9.

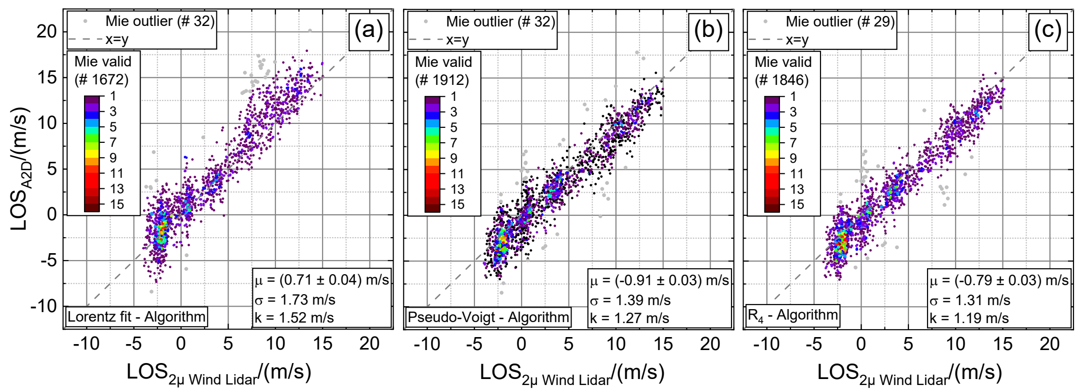

Fig. 9. A2D Mie LOS winds plotted against the 2-μm DWL wind speed projected onto the A2D LOS direction for the research flight performed on 16 September 2019 during the AVATAR-I campaign, analyzed with the (a) Lorentzian fit algorithm, (b) pseudo-Voigt fit algorithm, and (c) R_4 algorithm. Valid wind measurements are represented by colored dots, where the color indicates the frequency of data points at certain wind speeds on a 0.2×0.2 m/s grid (label). Outliers that exceeded a modified Z-score threshold of 3.5 are denoted by light-gray dots. The identity line is represented by the gray dashed line. The calculated bias [Eqs. (11) and (14)], the standard deviation [Eq. (12)], and the scaled MAD [Eq. (13)] are given by the respective insets.

Table 2. Comparison of Mie Winds Retrieved on 16 September 2019 with Different Algorithms

Algorithm	Valid Data Points	Outliers[a]	Random Error[b]/(m/s)
Lorentz	1672	32 (1.9%)	1.52
Pseudo-Voigt	1912 (14% more)	32 (1.7%)	1.27
R_4	1846 (10% more)	29 (1.6%)	1.19

[a]Outliers are defined as data points exceeding a modified Z-score of 3.5.
[b]The random error is given by the scaled MAD k.

The Lorentzian-based algorithm provides 5050 valid wind measurements and 180 outliers (3.7%). The determined bias is (0.14 ± 0.02) m/s, and the corresponding random error according to the scaled MAD is 1.50 m/s. The outliers (light-gray dots) represent a large positive bias for positive LOS winds and a negative bias for negative LOS winds. The root cause for this characteristic is currently unknown. Compared to that, the pseudo-Voigt-based algorithm provides 7519 valid wind measurements with 294 outliers (3.9%), an increase in data availability of 48.9%. This significant increase in valid winds clearly confirms the better performance of the pseudo-Voigt-based algorithm compared to the Lorentzian one. The determined bias is (-0.39 ± 0.02) m/s and the corresponding random error is 1.50 m/s and hence, equally high as for the Lorentzian-based analysis, although the number of valid wind measurements is significantly increased. Furthermore, it can be realized that the outliers are evenly distributed to positive and negative values, which also points to a better performance of the pseudo-Voigt-based algorithm. The R_4 algorithm provides 7578 valid wind measurements with 234 outliers (3.0%), which is very comparable to the pseudo-Voigt-based analysis with 50% more data points than the Lorentzian-based algorithm. The determined bias is (-0.25 ± 0.02) m/s and the corresponding random error is 1.60 m/s and thus, comparable to the other two algorithms. As mentioned before, the QC thresholds were set such that the random error for the different analyses is comparable. Thus, the increase in valid wind measurements can be directly considered as a better performance of the respective algorithm. Both the pseudo-Voigt as well as the R_4-based algorithm perform better than the Lorentzian-based one, which is likely due to the better representation of the actual Fizeau fringe profile. Hence, especially for applications that require a fast computation time, the novel R_4 algorithm is a very good alternative as it is one to two orders of magnitude faster than

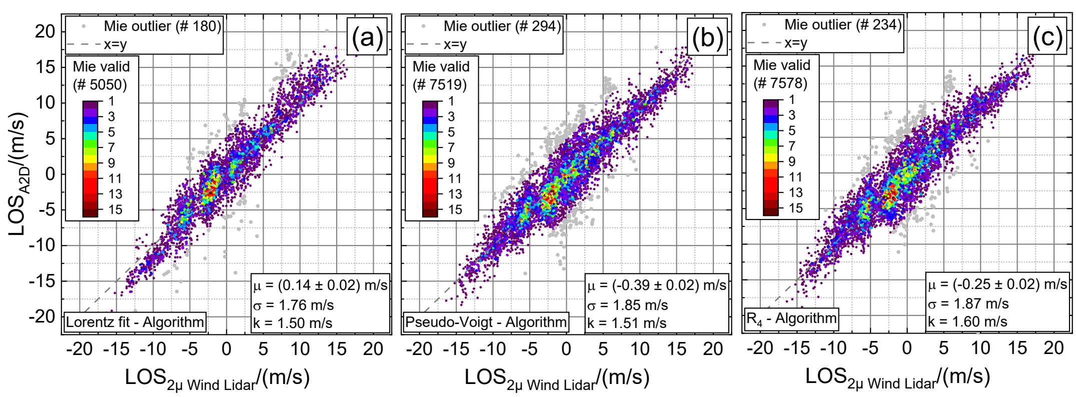

Fig. 10. Same as Fig. 9, but for all 10 research flights from the AVATAR-I campaign.

Table 3. Comparison of Mie Winds Retrieved with Different Algorithms

Algorithm	Valid Data Points	Outliers[a]	Random Error[b]/(m/s)
Lorentz	5050	180 (3.7%)	1.50
Pseudo-Voigt	7518 (49% more)	294 (3.9%)	1.50
R_4	7578 (50% more)	234 (3.0%)	1.60

[a]Outliers are defined as data points exceeding a modified Z-score of 3.5.
[b]The random error is given by the scaled MAD.

the fit-based algorithms. In the future, both the pseudo-Voigt as well as the R_4-based algorithms are foreseen to be applied to Aeolus data, to verify if a similar improvement can be reached. A summary of the performance of the different Mie fringe analysis algorithms for all 10 AVATAR-I flights is given in Table 3.

8. SUMMARY AND CONCLUSION

The Aeolus mission by ESA was launched in August 2018 and carried the direct-detection wind lidar ALADIN. To support Aeolus, the ALADIN Airborne Demonstrator (A2D) instrument was developed. Both ALADIN and A2D measure the LOS wind speed from both molecular and particulate backscatter signals in the Rayleigh and Mie channels. The Mie channel is based on the fringe-imaging technique, which relies on determining the spatial location of a fringe that originated in a Fizeau spectrometer. For this purpose, different fringe analysis algorithms can be applied. Based on A2D data acquired during 10 research flights performed in the framework of the AVATAR-I campaign, the performance of two algorithms using Lorentzian and the pseudo-Voigt-fit functions was investigated by comparing the retrieved wind speeds to reference data provided by the heterodyne-detection 2-µm DWL. In addition to that, a novel Mie fringe analysis algorithm (R_4) was developed that is not based on a fitting routine, but on a simple intensity ratio approach. As a result, the R_4 algorithm is one to two orders of magnitude faster than the fit-based algorithms. Furthermore, simulations were performed to demonstrate that the R_4 algorithm is rather insensitive to the accurate knowledge of the actual fringe profile. This is particularly beneficial in the case of ALADIN, which cannot accurately measure the fringe profile from space due to the varying ground albedo, the varying Rayleigh signal contribution in the range gate containing the ground return, and the uncertainties induced by the correction of the illumination function. It is shown that the R4 difference for different Lorentzian and Voigt profiles with FWHM varying from 150 to 200 MHz is only 0.7 MHz, which corresponds to a LOS wind speed of 0.12 m/s.

A statistical comparison of A2D data against 2-µm DWL data for all 10 research flights performed during AVATAR-I reveals that both the pseudo-Voigt-fit-based as well as the R_4-based analyses provide significantly better performance than the Lorentzian-fit-based analysis, resulting in 50% more valid data points with a similar random error. Hence, especially when fast computation times are required, the newly developed R_4 algorithm is a very good alternative to the pseudo-Voigt-fit-based algorithm.

In the future, it is planned to test both the pseudo-Voigt-fit-based algorithm as well as the R_4 also for the Aeolus wind retrieval to verify if similar significant improvements can be obtained. In addition, the R_4 algorithm will be used in the future for analyzing large data sets as it is for instance done for the determination of the laser frequency stability based on a single laser pulse analysis.

It is also worth mentioning that the R_4 algorithm can be adapted to other spectroscopic applications where sub-pixel knowledge of the location of measured peak profiles is needed. For this, the algorithm can also be adapted to various fringe profiles by modifying the calibration constants given in Eq. (9) accordingly.

Funding. Deutsches Zentrum für Luft- und Raumfahrt (ADM-III Verlängerung grant); European Space Agency (4000126336/18/I-BG, 4000128136/19/NL/IA, 4000129946/20/NL/IA).

Acknowledgment. The authors are grateful to the DLR flight experiments department, for the realization of the AVATAR-I airborne campaign, to Stephan Rahm (DLR) for processing and providing the 2-µm DWL data of the AVATAR-I campaign, as well as to Kevin Ridley (OLA) for detailed wave optic calculations of Fizeau profiles. The internal review of the paper draft manuscript by Sonja Gisinger (DLR) is highly appreciated.

Disclosures. The authors declare no conflicts of interest.

Data availability. The data presented in this paper are not publically available but can be requested from the authors.

REFERENCES

1. ESA, "The four candidate earth explorer core missions: Atmospheric dynamics mission," ESA Report for Mission Selection ESA SP- 1233 (1999), p. 145.
2. ESA, "ADM-Aeolus," Science report, ESA-SP-1311 (2008).
3. A. Stoffelen, J. Pailleux, E. Källén, J. M. Vaughan, L. Isaksen, P. Flamant, W. Wergen, E. Andersson, H. Schyberg, A. Culoma, R. Meynart, M. Endemann, and P. Ingmann, "The atmospheric dynamics mission for global wind field measurement," Bull. Am. Meteorol. Soc. **86**(1), 73–88 (2005).
4. O. Reitebuch, "The spaceborne wind lidar mission ADM-aeolus," in *Atmospheric Physics: Background—Methods—Trends*, U. Schumann, ed. (Springer Berlin, 2012), p. 877.
5. T. Kanitz, J. Lochard, J. Marshall, P. McGoldrick, O. Lecrenier, P. Bravetti, O. Reitebuch, M. Rennie, D. Wernham, and A. Elfving, "Aeolus first light: first glimpse," Proc. SPIE **11180**, 111801R (2019).
6. O. Reitebuch, C. Lemmerz, O. Lux, *et al.*, "Initial assessment of the performance of the first Wind Lidar in space on Aeolus," EPJ Web Conf. **237**, 01010 (2020).
7. A.-G. Straume, M. Rennie, L. Isaksen, *et al.*, "ESA's Space-based Doppler wind lidar mission aeolus—first wind and aerosol product assessment results," EPJ Web Conf. **237**, 1007 (2020).
8. M. Weissmann and C. Cardinali, "Impact of airborne Doppler lidar observations on ECMWF forecasts," Q. J. R. Meteorol. Soc. **133**, 107–116 (2007).
9. D. G. Tan, E. Andersson, M. Fisher, and L. Isaksen, "Observing-system impact assessment using a data assimilation ensemble technique: application to the ADM-Aeolus wind profiling mission," Q. J. R. Meteorol. Soc. **133**, 381–390 (2007).
10. G.-J. Marseille, A. Stoffelen, and J. Barkmeijer, "Impact assessment of prospective spaceborne doppler wind lidar observation scenarios," Tellus A **60**, 234–248 (2008).
11. A. Horányi, C. Cardinali, M. Rennie, and L. Isaksen, "The assimilation of horizontal line-of-sight wind information into the ECMWF data assimilation and forecasting system. Part I: the assessment of wind impact," Q. J. R. Meteorol. Soc. **141**, 1223–1232 (2015).
12. M. Rennie and L. Isaksen, *The NWP Impact of Aeolus Level-2B Winds at ECMWF* (ECMWF, 2020).
13. M. P. Rennie, L. Isaksen, F. Weiler, J. de Kloe, T. Kanitz, and O. Reitebuch, "The impact of Aeolus wind retrievals on ECMWF global weather forecasts," Q. J. R. Meteorol. Soc. **147**, 3555–3586 (2021).

14. W. E. Baker, R. Atlas, C. Cardinali, *et al.*, "Lidar-measured wind profiles: the missing link in the global observing system," Bull. Am. Meteorol. Soc. **95**, 543–564 (2014).
15. U. Paffrath, C. Lemmerz, O. Reitebuch, B. Witschas, I. Nikolaus, and V. Freudenthaler, "The airborne demonstrator for the direct-detection Doppler wind lidar ALADIN on ADM-Aeolus. Part II: simulations and Rayleigh receiver radiometric performance," J. Atmos. Oceanic Technol. **26**, 2516–2530 (2009).
16. O. Reitebuch, C. Lemmerz, E. Nagel, U. Paffrath, Y. Durand, M. Endemann, F. Fabre, and M. Chaloupy, "The airborne demonstrator for the direct-detection Doppler wind lidar ALADIN on ADM-Aeolus. Part I: instrument design and comparison to satellite instrument," J. Atmos. Oceanic Technol. **26**, 2501–2515 (2009).
17. U. Marksteiner, C. Lemmerz, O. Lux, S. Rahm, A. Schäfler, B. Witschas, and O. Reitebuch, "Calibrations and wind observations of an airborne direct-detection wind LiDAR supporting ESA's aeolus mission," Remote Sens. **10**, 2056 (2018).
18. O. Lux, C. Lemmerz, F. Weiler, U. Marksteiner, B. Witschas, S. Rahm, A. Schäfler, and O. Reitebuch, "Airborne wind lidar observations over the North Atlantic in 2016 for the pre-launch validation of the satellite mission Aeolus," Atmos. Meas. Tech. **11**, 3297–3322 (2018).
19. C. Lemmerz, O. Lux, B. Witschas, S. Rahm, U. Marksteiner, A. Geiß, F. Weiler, and O. Reitebuch, "Airborne Doppler wind LIDAR technology demonstration for Aeolus: from pre-launch campaigns to mission performance validation," Proc. SPIE **12777**, 72–84 (2023).
20. B. Witschas, C. Lemmerz, A. Geiß, O. Lux, U. Marksteiner, S. Rahm, O. Reitebuch, and F. Weiler, "First validation of Aeolus wind observations by airborne Doppler wind lidar measurements," Atmos. Meas. Tech. **13**, 2381–2396 (2020).
21. B. Witschas, C. Lemmerz, A. Geiß, O. Lux, U. Marksteiner, S. Rahm, O. Reitebuch, A. Schäfler, and F. Weiler, "Validation of the Aeolus L2B wind product with airborne wind lidar measurements in the polar North Atlantic region and in the tropics," Atmos. Meas. Tech. **15**, 7049–7070 (2022).
22. O. Lux, C. Lemmerz, F. Weiler, U. Marksteiner, B. Witschas, S. Rahm, A. Geiß, and O. Reitebuch, "Intercomparison of wind observations from the European Space Agency's Aeolus satellite mission and the ALADIN Airborne Demonstrator," Atmos. Meas. Tech. **13**, 2075–2097 (2020).
23. O. Lux, C. Lemmerz, F. Weiler, U. Marksteiner, B. Witschas, S. Rahm, A. Geiß, A. Schäfler, and O. Reitebuch, "Retrieval improvements for the ALADIN Airborne Demonstrator in support of the Aeolus wind product validation," Atmos. Meas. Tech. **15**, 1303–1331 (2022).
24. J. A. McKay, "Assessment of a multibeam Fizeau wedge interferometer for Doppler wind lidar," Appl. Opt. **41**, 1760–1767 (2002).
25. O. Reitebuch, D. Huber, and I. Nikolaus, "ADM-aeolus algorithm theoretical basis document (ATBD)—Level 1B products," AE.RP.DLR.L1B.001 (2018), p. 117.
26. M. Rennie, D. Tan, E. Andersson, P. Poli, A. Dabas, J. De Kloe, G.-J. Marseille, and A. Stoffelen, *Aeolus Level-2B Algorithm Theoretical Basis Document (Mathematical Description of the Aeolus Level-2B Processor)* (ECMWF, 2020).
27. O. Lux, C. Lemmerz, F. Weiler, T. Kanitz, D. Wernham, G. Rodrigues, A. Hyslop, O. Lecrenier, P. McGoldrick, F. Fabre, P. Bravetti, T. Parrinello, and O. Reitebuch, "ALADIN laser frequency stability and its impact on the Aeolus wind error," Atmos. Meas. Tech. **14**, 6305–6333 (2021).
28. L.-S. Lee and A. L. Schawlow, "Multiple-wedge wavemeter for pulsed lasers," Opt. Lett. **6**, 610–612 (1981).
29. S. Kobtsev, S. Kandrushin, and A. Potekhin, "New approach to long-term frequency stabilisation of radiation of single-frequency lasers," Proc. SPIE **6731**, 67312U (2007).
30. J. J. Snyder, "Algorithm for fast digital analysis of interference fringes," Appl. Opt. **19**, 1223–1225 (1980).
31. D. A. Landman, R. Roussel-Dupre, and G. Tanigawa, "On the statistical uncertainties associated with line profile fitting," Astrophys. J. **261**, 732–735 (1982).
32. O. Lardière, R. Conan, R. Clare, C. Bradley, and N. Hubin, "Performance comparison of centroiding algorithms for laser guide star wavefront sensing with extremely large telescopes," Appl. Opt. **49**, G78–G94 (2010).
33. E. Jacobsen and P. Kootsookos, "Fast, accurate frequency estimators [DSP Tips & Tricks]," IEEE Signal Process. Mag. **24**(3), 123–125 (2007).
34. M. Weissmann, R. Busen, A. Dörnbrack, S. Rahm, and O. Reitebuch, "Targeted observations with an airborne wind lidar," J. Atmos. Ocean. Technol. **22**, 1706–1719 (2005).
35. B. Witschas, S. Rahm, A. Dörnbrack, J. Wagner, and M. Rapp, "Airborne wind lidar measurements of vertical and horizontal winds for the investigation of orographically induced gravity waves," J. Atmos. Ocean. Technol. **34**, 1371–1386 (2017).
36. B. Witschas, S. Gisinger, S. Rahm, A. Dörnbrack, D. C. Fritts, and M. Rapp, "Airborne coherent wind lidar measurements of the momentum flux profile from orographically induced gravity waves," Atmos. Meas. Tech. **16**, 1087–1101 (2022).
37. O. Reitebuch, D. Huber, and I. Nikolaus, "Algorithm theoretical basis document ATBD: ADM-aeolus level 1b products," Tech. Rep., AE-RP-DLR-L1B-001 (2014).
38. O. Lux, D. Wernham, P. Bravetti, P. McGoldrick, O. Lecrenier, W. Riede, A. D'Ottavi, V. De Sanctis, M. Schillinger, J. Lochard, J. Marshall, C. Lemmerz, F. Weiler, L. Mondin, A. Ciapponi, T. Kanitz, A. Elfving, T. Parrinello, and O. Reitebuch, "High-power and frequency-stable ultraviolet laser performance in space for the wind lidar on Aeolus," Opt. Lett. **45**, 1443–1446 (2020).
39. B. Witschas, C. Lemmerz, O. Lux, U. Marksteiner, O. Reitebuch, F. Weiler, F. Fabre, A. Dabas, T. Flament, D. Huber, and M. Vaughan, "Spectral performance analysis of the Aeolus Fabry–Pérot and Fizeau interferometers during the first years of operation," Atmos. Meas. Tech. **15**, 1465–1489 (2022).
40. M. Chanin, A. Garnier, A. Hauchecorne, and J. Porteneuve, "A Doppler lidar for measuring winds in the middle atmosphere," Geophys. Res. Lett. **16**, 1273–1276 (1989).
41. C. Flesia and C. Korb, "Theory of the double-edge molecular technique for Doppler lidar wind measurement," Appl. Opt. **38**, 432–440 (1999).
42. A. Schäfler, G. Craig, H. Wernli, *et al.*, "The North Atlantic waveguide and downstream impact experiment," Bull. Am. Meteorol. Soc. **99**(8), 1607–1637 (2018).
43. F. Chouza, B. Witschas, and O. Reitebuch, "Heterodyne high-spectral-resolution lidar," Appl. Opt. **56**, 8121–8134 (2017).
44. J. Wagner, A. Dörnbrack, M. Rapp, S. Gisinger, B. Ehard, M. Bramberger, B. Witschas, F. Chouza, S. Rahm, C. Mallaun, G. Baumgarten, and P. Hoor, "Observed versus simulated mountain waves over Scandinavia—improvement of vertical winds, energy and momentum fluxes by enhanced model resolution?" Atmos. Chem. Phys. **17**, 4031–4052 (2017).
45. S. Gisinger, J. Wagner, and B. Witschas, "Airborne measurements and large-eddy simulations of small-scale gravity waves at the tropopause inversion layer over scandinavia," Atmos. Chem. Phys. **20**, 10091–10109 (2020).
46. K. Browning and R. Wexler, "The determination of kinematic properties of a wind field using Doppler radar," J. Appl. Meteorol. **7**, 105–113 (1968).
47. T. Fujii and T. Fukuchi, *Laser Remote Sensing* (CRC Press, 2005).
48. O. Lux, B. Witschas, A. Geiß, C. Lemmerz, F. Weiler, U. Marksteiner, S. Rahm, A. Schäfler, and O. Reitebuch, "Quality control and error assessment of the Aeolus L2B wind results from the Joint Aeolus Tropical Atlantic Campaign," Atmos. Meas. Tech. **15**, 6467–6488 (2022).
49. M. Born and E. Wolf, *Principles of Optics: Electromagnetic Theory of Propagation, Interference and Diffraction of Light* (Pergamon, 1980).
50. J. M. Vaughan, *The Fabry-Perot Interferometer* (Adam Hilger, 1989).
51. T. Kajava, H. Lauranto, and A. Friberg, "Interference pattern of the Fizeau interferometer," J. Opt. Soc. Am. A **11**, 2045–2054 (1994).
52. W. Voigt, "Über das Gesetz der Intensitätsverteilung innerhalb der Linien eines Gasspektrums," in *Sitzungsberichte*, München, Germany, 1912, Vol. **25**.
53. E. Jakeman and K. D. Ridley, *Modeling Fluctuations in Scattered Waves* (CRC Press, 2006).
54. N. Hagen, M. Kupinski, and E. Dereniak, "Gaussian profile estimation in one dimension," Appl. Opt. **46**, 5374–5383 (2007).

55. U. Marksteiner, "Airborne wind lidar observations for the validation of the ADM-Aeolus instrument," Ph.D. thesis (Technische Universität München, 2013).
56. U. Marksteiner, O. Reitebuch, S. Rahm, I. Nikolaus, C. Lemmerz, and B. Witschas, "Airborne direct-detection and coherent wind lidar measurements along the east coast of Greenland in 2009 supporting ESA's Aeolus mission," Proc. SPIE **8182**, 116–123 (2011).
57. B. Iglewicz and D. C. Hoaglin, *How to Detect and Handle Outliers* (Asq, 1993), Vol. **16**.
58. G.-J. Marseille, J. de Kloe, U. Marksteiner, O. Reitebuch, M. Rennie, and S. de Haan, "NWP calibration applied to Aeolus Mie channel winds," Q. J. R. Meteorol. Soc. **148**, 1020–1034 (2022).